Fractography of Cold Crack of Various Carbon Steels and Alloy Steels by Means of the Implant Test†

—Studies on Fractography of Welded Zone (IV)—

Fukuhisa MATSUDA*, Hiroji NAKAGAWA, Tatsuo TSUJI*** and Muneyasu TSUKAMOTO*****

Abstract

Fractographic investigation is made on weld cold crack of various plain carbon steels and alloy steels, using the implant cracking test in different diffusible hydrogen contents and observing by a scanning electron microscope. Main conclusions obtained are as follows: (1) Fracture mode of hydrogen-induced delayed crack dominates in plain carbon steels whose carbon content is less than about 0.50% and in weldable high strength steels. (2) Fracture mode of quenching crack together with hydrogen-induced delayed crack is obvious in plain carbon steels whose carbon content is more than about 0.50% and in medium carbon low alloy steels. (3) Fracture surface consists of three or four modes among intergranular, quasi-cleavage, cleavage and dimple fractures. Decrease in applied stress increases the area of quasi-cleavage fracture mode in all specimens, where tear ridges and secondary cracks are formed due to hydrogen. Increase in applied stress increases the area of dimple fracture mode in steels described in (1) and intergranular fracture mode in steels described in (2).

1. Introduction

Cold crack of steels is one of the most serious ploblems that are encountered during welding performance. It is generally known that cold crack of low carbon steels and low carbon low alloy steels are mainly due to hydrogen-induced delayed crack. Therefore, there are many reports[1),2)] which deal with hydrogen embrittlement in relation to alloy elements, microstructure, weld heat input, diffusible hydrogen content, restraint stress and so on.

Recently, fractographic investigations on hydrogen-induced crack have been reported.[3),4),5)] According to their results, the fracture mode is changed from intergranular one into quasi-cleavage one, and further into dimple one as the stress intencity factor increases.

However, it has been yet obscure as regards the effects of microstructure, alloy elements, diffusible hydrogen content and so on.

On the other hand, it is reported[6)] that cold crack not showing the behavior of delayed crack occurs in welding of middle carbon low alloy steels, and that the crack predominently passes along the prior austenitic grain boundaries. This type crack is considered to be a kind of quenching crack caused by martensitic transformation. However, it is not quite obvious in what chemical composition this type crack occurs.

Recently the implant cracking test[7)] has been widely used, since it is enable to easily study the relation between applied stress and fracture time.

In this report, the implant cracking test has been applied to cold cracking test of low carbon steels, weldable high strength steels of low carbon low alloy, middle carbon steels, high carbon steels, middle carbon low alloy steels and high carbon low alloy steel, varying diffusible hydrogen content and applied stress. Then their fracture surfaces have been observed in detail with a scanning electron microscope.

2. Materials Used and Experimental Procedure

2.1 Materials Used

Materials used are as follows:

Plain carbon steels; JIS※ S20C(corresponding to AISI 1020), S35C(1035), S48C(1045), S50C(1050), S55C(1055) and SK3※※(AISI W1) Weldable high strength steels; 50 kg/mm² class of tensile strength—JIS SM50(Mn-Si type, ASTM A242-70a), 60 kg/mm² class of tensile strength—HT60(heat-treated type,

† Received on April 17, 1978
* Professor
** Research Instructor
*** Sumikin Welding Electrode Co., LTD.
※ Japan Industrial Standard
※※ Carbon tool steel

ASTM A440-70a) and 80 kg/mm² class of tensile strength—HT80(heat-treated type, T-1 type)
Chromium-Molybdeum steel; JIS SCM4(AISI 4140)
Nickel-Chromium-Molybdeum steel; JIS SNCM8 (AISI 4340)
High Carbon-Chromium bearing steel; JIS SUJ2 (ASTM A295-61B)

Their chemical compositions are summarized in **Table 1.** Table 1 also contains carbon equivalent Ceq of each material which is defined in JIS for low carbon low alloy steels, though the applicability of Ceq is doubtful for all the materials used in this paper.

Four types of covered electrodes were used which were different each other in their diffusible hydrogen contents. The diffusible hydrogen contents were changed by controlling the content of hydrated mineral in basic lime flux or by using ilmenite type flux, and they are shown in **Table 2,** which were measured by the IIW procedure. The contents of 3.4, 5.7, 16.1 and 43.7 ml/100 g of deposited metal are hereafter marked as H-I, H-II, H-III and H-IV respectively. Tensile strength of the deposited metal from the electrodes I, II and III is 50 kg/mm² class, and that from the electrode IV is 40 kg/mm² class.

2.2 The Implant Cracking Test

2.2.1 Configuration of Specimen

Specimen of the implant cracking test was 6 mm in diameter, which was machined with the axis parallel to the direction of hot working. Then, a helical notch conceived by W. F. Savage et al.[8] was machined in order to avoid scattering of data due to an error of fusion penetration, the detail of which is illustrated in **Fig. 1.**

2.2.2 Testing Procedure

General appearance of the implant testing apparatus is shown in **Fig. 2,** where load is applied by a lever and a dead weight, and the applied load is changeable up to 5 ton by varying the dead weight.

A backing plate(JIS SM50) of 22 mm thick ×200mm wide ×300 mm long was used, and test welding was done on the backing plate. The welding condition are 25V of arc voltage, 170 A of welding current, 150 mm/min of welding speed, that is 17 kJ/cm of

Table 1 Chemical compositions of materials used

Steel	Chemical composition (wt. %)										Ceq*	Thickness	Diameter
	C	Si	Mn	P	S	Cu	Ni	Cr	Mo	V		(mm)	(mm)
S20C	0.21	0.05	0.42	0.013	0.051	—	—	—	—	—	0.28	—	16
S35C	0.32	0.22	0.67	0.027	0.019	0.01	0.02	0.03	0.01	0.002	0.44	—	19
S48C	0.49	0.21	0.78	0.028	0.026	0.02	0.02	0.03	0.01	0.002	0.64	—	22
S50C	0.52	0.25	0.84	0.019	0.013	0.02	0.02	0.11	0.01	<0.01	0.69	—	16
S55C	0.54	0.31	0.79	0.022	0.021	0.02	0.05	0.13	<0.01	<0.01	0.71	—	13
SK3	1.00	0.38	0.45	0.011	0.009	0.05	0.07	0.12	0.08	—	1.14	—	13
SM50	0.16	0.50	1.39	0.012	0.009	0.02	0.02	0.01	<0.01	<0.01	0.41	16	—
HT60	0.14	0.31	1.28	0.015	0.015	0.02	0.02	0.03	0.01	0.05	0.37	25	—
HT80	0.13	0.27	0.86	0.011	0.004	0.25	1.08	0.50	0.43	0.004	0.52	25	—
SCM4	0.38	0.19	0.69	0.018	0.002	0.03	0.02	0.94	0.17	<0.01	0.73	—	55
SNCM8	0.42	0.31	0.70	0.017	0.025	0.14	1.71	0.75	0.15	<0.01	0.78	—	60
SUJ2	1.01	0.28	0.38	0.007	0.011	0.06	0.03	1.36	0.01	<0.01	1.36	—	13

* Ceq=C+1/6Mn+1/24Si+1/40Ni+1/5Cr+1/4Mo+1/14 V (wt.%)

Table 2 Diffusible hydrogen contents of electrodes used and drying condition of electrodes

Mark	Electrode				Drying condition	Diffusible hydrogen content	
	Class		Type of coating	Diameter (mm)			
	JIS	AWS				mlNTP/100 g	Mark
E-I	D5016	E7016	Basic lime	4	350°C×1hr	3.4	H-I
E-II	D5016	E7016	Basic lime	4	350°C×1hr	5.7	H-II
E-III	D5016	E7016	Basic lime	4	250°C×1hr	16.1	H-III
E-IV	D4301	—	Ilmenite	4	150°C×1hr	43.7	H-IV

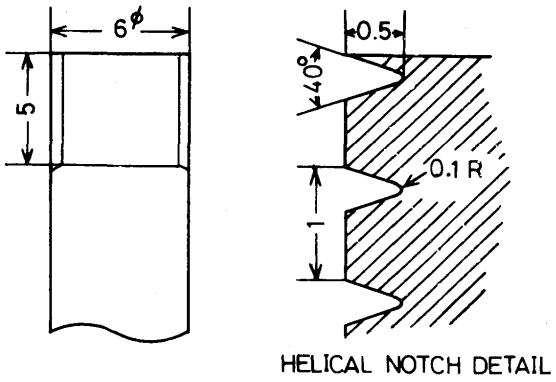

Fig. 1 Implant specimen details

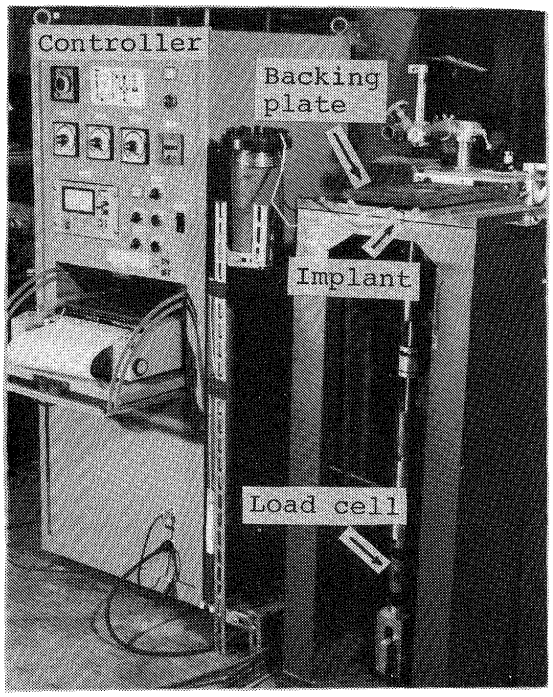

Fig. 2 General appearance of implant testing apparatus

weld heat input, and 100 mm of bead-on-plate weld length. The cooling time between 800 and 500°C was about 6 sec. Then setted load was applied to the specimen at 1 min after the test weld was completed, when the temperature around the helical notch of the specimen was about 120 to 150°C. The maximum testing time was limited to 24 hrs.

2.2.3 Observation of Fracture Surface

Fracture surface was observed in detail with a scanning electron microscope (SEM). If need were, the element on fracture surface was analyzed with an energy dispersive type analyzer (EDX) attached to the SEM. Moreover, direct correspondence between fracture surface and microstructure was partly examined by the procedure reported by F. Terasaki et al.[9].

3. Experimental Results

3.1 Microstructure of Heat-Affected Zone

Typical microstructures of heat-affected zone near the fusion boundary are shown in **Fig. 3,** as observed in light microscope.

The microstructure of S20C, Fig. 3(a), was composed of proeutectoid ferrite and upper-bainite formed at the grain boundaries of prior austenite, and of the rest of the matrix mainly transformed to bainite and martensite.

The microstructures of S35C and S48C, Fig. 3(b) and 3(c), were composed of troostite and sporadic upper-bainite at the grain boundaries of prior austenite, and of the rest of the matrix mainly transformed to martensite.

The microstructures of S50C and S55C, Fig. 3(d) and 3(e), were composed of upper-bainite and sporadic troostite at grain boundaries of prior austenite, and of the rest of the matrix mainly transformed to martensite.

The microstructure of SM50, Fig. 3(g), was composed of sporadic ferrite and upper-bainite formed at the grain boundaries of prior austenite and the rest of the matrix transformed to martensite.

The microstructure of HT60, Fig. 3(h), was sporadic upper-bainite formed at the grain boundaries of prior austenite and the rest of the matrix transformed to martensite.

The microstructure of HT80, Fig. 3(i), was mainly composed of martensite only.

The martensite structures of the specimens mentioned above were lath-like martensite.

The microstructures of SCM4 and SNCM8, Fig. 3(j) and 3(k), were mainly composed of lath-like martensite and partly of acicular martensite. As shown in Fig. 3(j), the microstructure of SCM4 was hardly etched at the grain boundaries. Then, a line analysis of EPMA was made to SCM4. The result showed that chromium was enriched at the grain boundaries.

The microstructures of SK3 and SUJ2, Fig. 3(f) and 3(l), were composed of acicular martensite and retained austenite. The plates of acicular martensite were different each other in the size and the orientation. Besides, microcracks which was reported by A.R. Marder et al.[10] were occasionally observed at the impingement of plates even in the condition without applied stress as seen in Fig. 3(f). The microcrack tendency of SK3 was higher than that of SUJ2. However, marked intergranular crack was observed in SUJ2 without applied stress, as seen in Fig. 3(l).

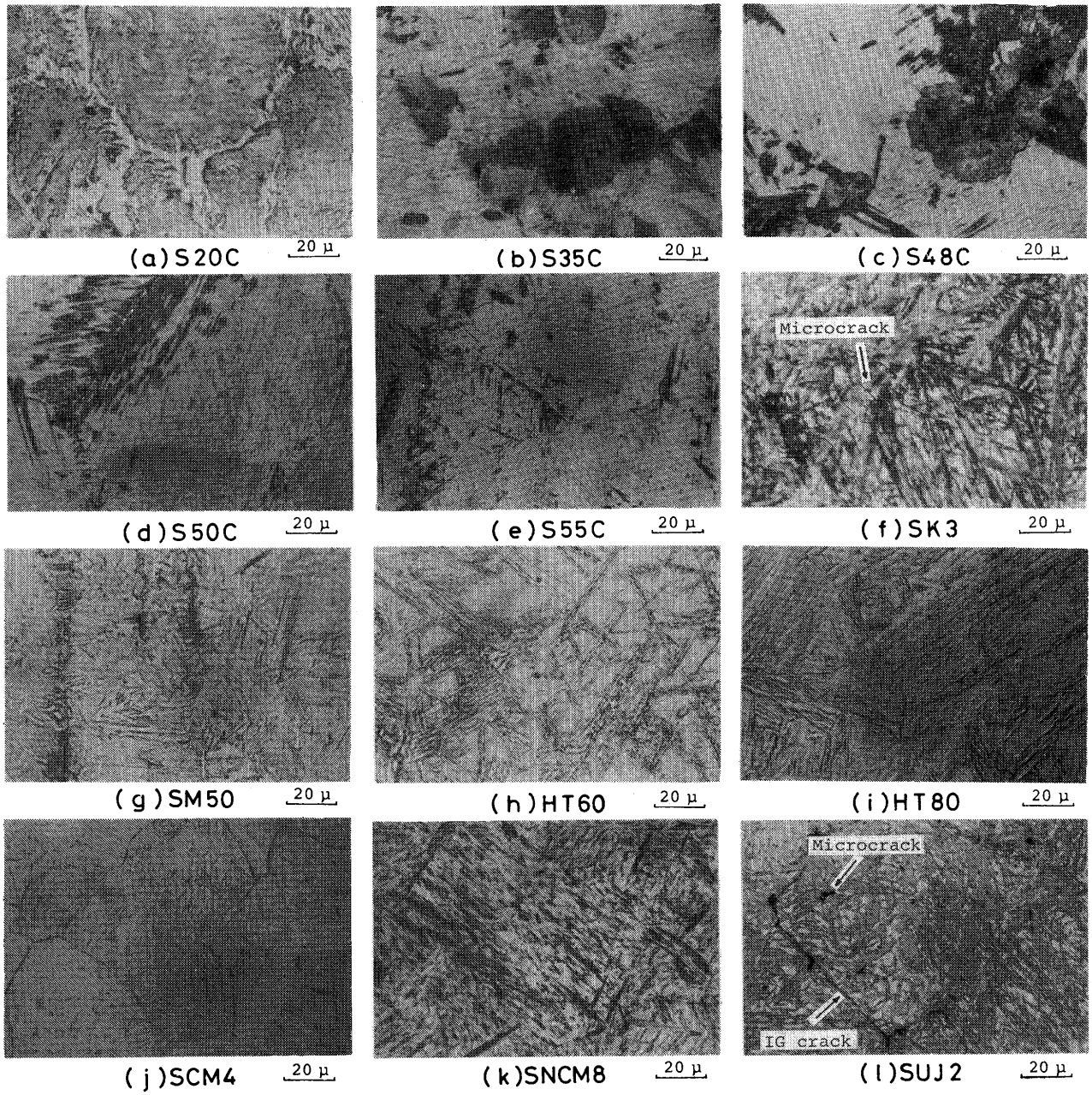

Fig. 3 Microstructures of heat-affected zone, echant; saturated aqueous picric acid with wetting agent

Figure 4 shows dependence of maximum hardness in the heat-affected zone on the carbon equivalent Ceq in Table 1, though the applicability of Ceq for all steels used in this paper is exceeded the limit of JIS regulation. A linear relation between the Ceq and the maximum hardness exists up to about 0.7 of Ceq, but the maximum hardness nearly saturates above about 0.7.

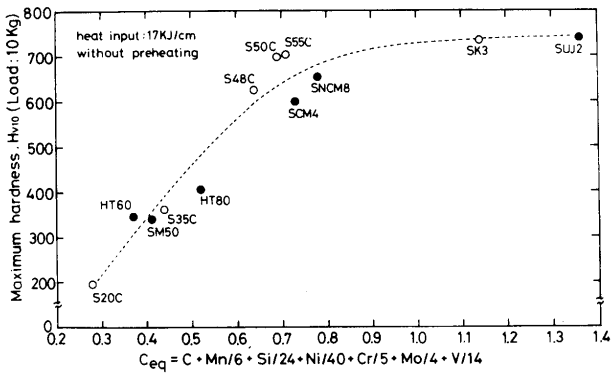

Fig. 4 Relation between Ceq and maximum hardness of heat-affected zone

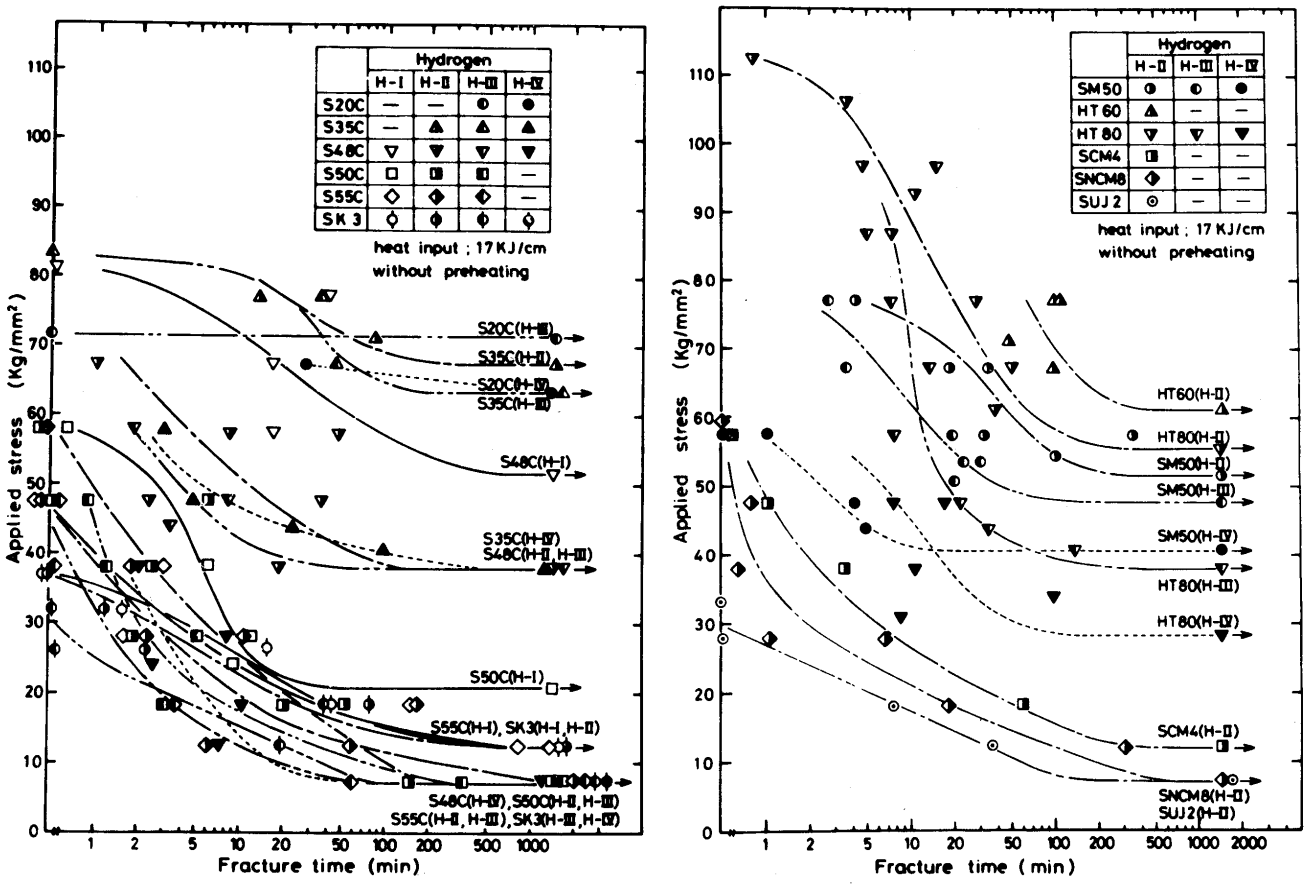

(a) (b)

Fig. 5 Relation between applied stress and fracture time
(a) Plain carbon steels
(b) High strength steels and middle and high carbon low alloy steels

3.2 Lower Critical Stress

Relation between the applied stress and the fracture time of all the specimens are summarized in **Fig. 5,** where Fig. 5(a) shows the results of plain carbon steels and Fig. 5(b) does those of alloy steels. Each relation is similar to that in delayed crack except for S20C in H-III of diffusible hydrogen. Increase in carbon of plain carbon steels or in diffusible hydrogen content generally decreases the lower critical stress. However, the lower critical stress is very low in plain carbon steels whose carbon content are not less than in S50C and in alloy steels SCM4, SNCM8 and SUJ2.

Relation between the diffusible hydrogen content and the lower critical stress for several steels are shown in **Fig. 6.** Increase in hydrogen content gradually decreases the lower critical stress of S20C, S35C, S48C, SM50 and HT80. However, the lower critical stress of S50C, S55C and SK3 is very low even in the extremely low hydrogen, and there is little dependence of the lower critical stress on the hydrogen content except for extremely low hydrogen region. These suggest that another factor, perhaps quenching crack, acts on fractures of S50C etc. together with delayed crack. The maximum hardness of this kind of steel is about above 600 according to Fig. 4.

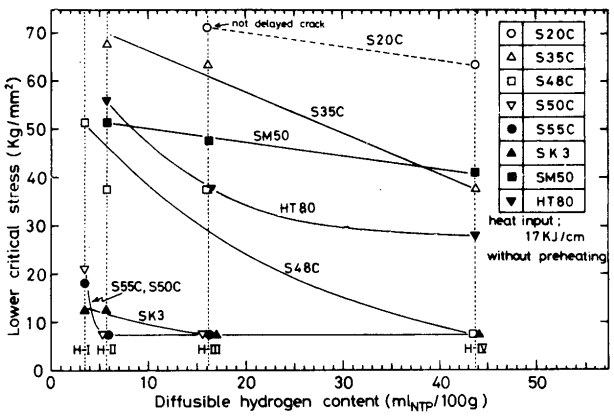

Fig. 6 Relation between diffusible hydrogen content and lower critical stress

3.3 Fractography

It has been supposed in the previous section that quenching crack together with delayed crack acts on the fracture of steels whose maximum hardness is very high, and this shall be recoginized from fractographic study in this section. Therefore, steels have been classified into Groups A and B. The Group A consists of S20C, S35C, S48C, SM50 and HT80, on which only hydrogen-induced delayed crack is considered to act. The Group B consists of S50C, S55C, SK3, SCM4, SNCM8 and SUJ2, on which quenching crack together with hydrogen-induced delayed crack is considered to act.

3.3.1 Fractography of Group A

Fracture surface of a steel in Group A consisted of three or four modes among intergranular, quasi-cleavage, cleavage and dimple fractures.

(a) Intergranular Fracture

Figure 7 shows the typical example of intergranular

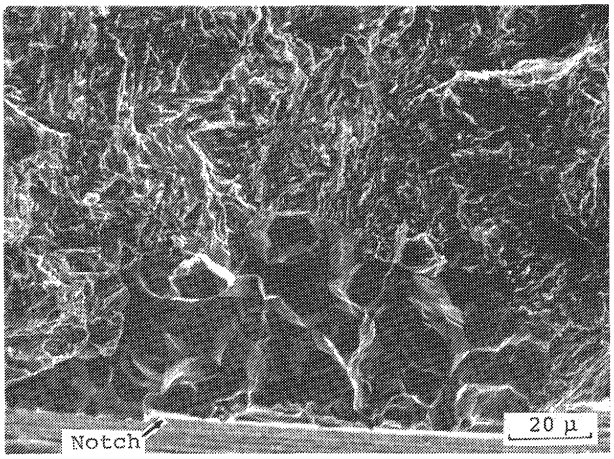

Fig. 7 Microfractograph of intergranular region in HT80, applied stress σ=96.7 kg/mm², fracture time Tf=4.5 min, diffusible hydrogen content Hd=5.7 ml/100 g

fracture occurred in HT80, where the intergranular fracture was observed in wide-ranging condition. As seen in Fig. 7, the intergranular fracture was formed in extremely narrow region in close vicinity to the notch, and was observed little or nothing in other region. Fracture mode around the intergranular fracture region was quasi-cleavage nextly mentioned. Macrofractographs and their sketches in **Fig. 8** show that the intergranular (IG) did not occur in a extremely high applied stress and that the IG region was limited to a very small area near the notch even in a lower applied stress. It is well known[3),5)] that the fracture mode in delayed crack is intergranular type in the lowest stress intencity factor. Therefore, the intergranular fracture region in close vicinity to the notch as

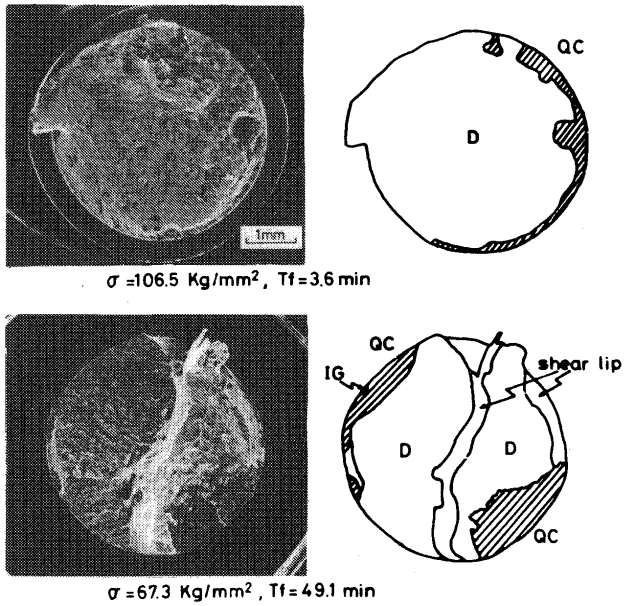

Fig. 8 Variation of macrofractograph of HT80 with decreasing applied stress, Hd=5.7 ml/100 g

seen in Fig. 7 is considered to be the crack-initiated part, since the stress intencity factor increases together with the crack propagation in the implant cracking test due to the constant load.

On the other hand, there was no intergranular fracture around the notch in S20C, S48C, SM50 and HT60. Figure 3 already mentioned shows that troostite and/or proeutectoid ferrite was generally formed at the prior austenitic grain boundaries in these steels. Thus, it is difficult to define the prior austenitic grain boundaries, and this may be the reason why the intergranular fracture was not observed. However, an interesting phenomenon was observed as regards SM50. That is, intergranular fractures were observed along lamellar segregation of non-metallic inclusions as seen in **Fig. 9.** Examples of the microfractographs are shown in **Fig. 10.** In Fig. 10(a) intergranular fractures are formed at both sides of hollows or secondary cracks due to lamellar segregation. In Fig. 10(b) intergranular fractures are

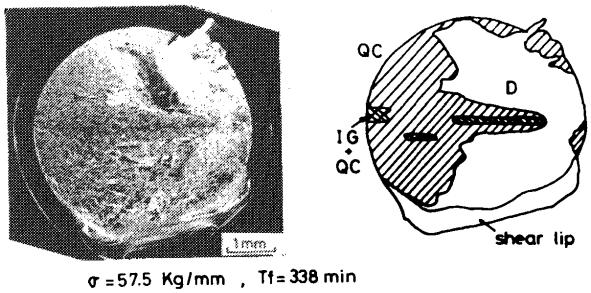

Fig. 9 Typical macrofractograph of SM50, Hd=5.7 ml/100 g

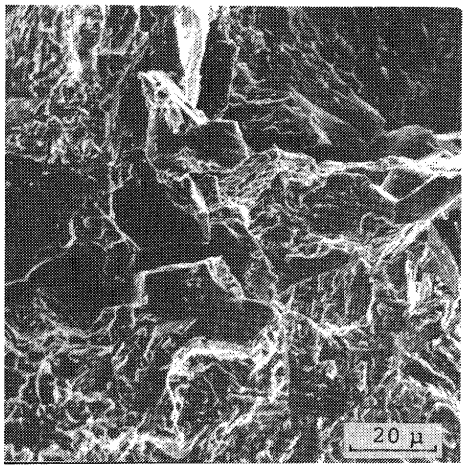

(a)

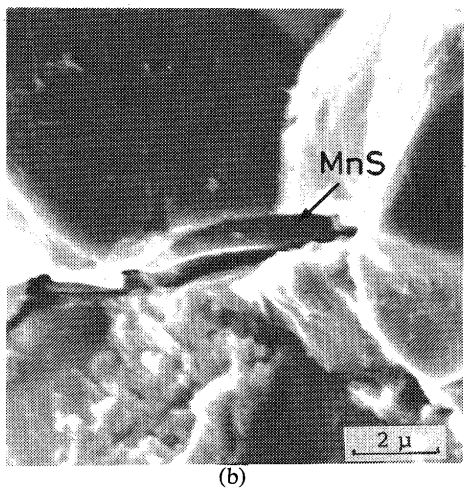

(b)

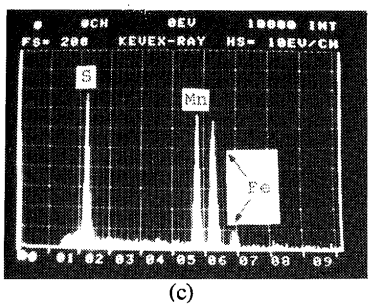

(c)

Fig. 10 Microfractograph of intergranular region along lamellar segregation in SM50, $\sigma=57.5$ kg/mm^2, Tf=30.6 min, Hd=5.7 ml/100 g
(a) Intergranular fracture along lamellar segregation
(b) Inclusion at grain boundary
(c) The EDX result of the inclusion in (b)

formed at both sides of a plate-like inclusion and the inclusion is identified to be MnS according to Fig. 10(c) of EDX analysis. Non-metallic inclusions in lamellar segregation are generally formed regardless of grain boundary. Therefore, Fig. 10 suggests that the non-metallic inclusion melted by welding thermal cycle penetrated the grain boundary. This can be confirmed in **Fig. 11,** where small inclusions observed at austenitic grain boundaries near the fusion boundary. Therefore, it is supposed that the concentrating of diffusible hydrogen due to a trap effect at the circumference of the inclusions and the drop of grain boundary strength due to the inclusion bring about the intergranular fracture along the lamellar segregation.

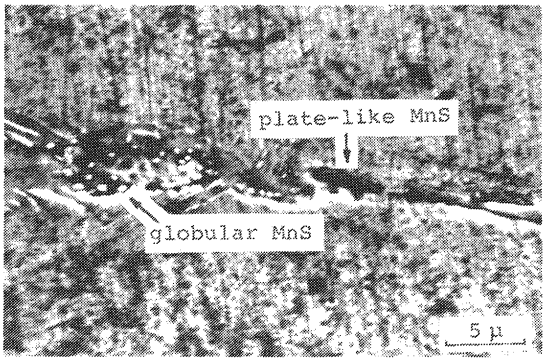

Fig. 11 Microstructure of SM50 by SEM, $\sigma=67.3$ kg/mm^2, Tf=34.2 min, Hd=5.7 ml/100 g

(b) Quasi-Cleavage Fracture

Quasi-cleavage fracture was observed in all the specimens and the general examples are shown in **Fig. 12**(a), (b) and (c). Since secondary cracks and tear ridges[4] due to martensite lath were observed, the quasi-cleavage fracture is considered to be effected by hydrogen. The quasi-cleavage region was generally formed about the notch as seen in Fig. 8, and decrease in the applied stress increased the area. Besides, intermingled fracture of quasi-cleavage and dimple as shown in Fig. 12(d) was frequently observed about the boundaries of quasi-cleavage and dimple regions, though the quantity was generally small. This intermingled fracture mode was generally formed in the weld metal.

(c) Dimple Fracture

Dimple fracture was observed in all the specimens and the example is shown in **Fig. 13**(a). The dimple region frequently passed through the weld metal near the fusion boundary, though it sometimes formed at the heat-affected zone. It is considered that the dimple whose inclusion was enriched with S and Mn as shown in Fig. 13(b) was formed in the heat-affected zone and that the dimple whose inclusion was enriched with Al, Si, Ti and Mn as shown in Fig. 13(c) was formed in the weld metal. Shear dimples were formed in shear lip zone seen in Fig. 8.

Besides, ductile intergranular fracture was sometimes observed within the dimple region of S48C as seen in **Fig. 14** and the inclusion in dimple was MnS type. It is supposed that the MnS type inclusion melted by welding thermal cycle penetrated the grain boundary and thus the weakened grain boundary fractured at the final rapid fracture.

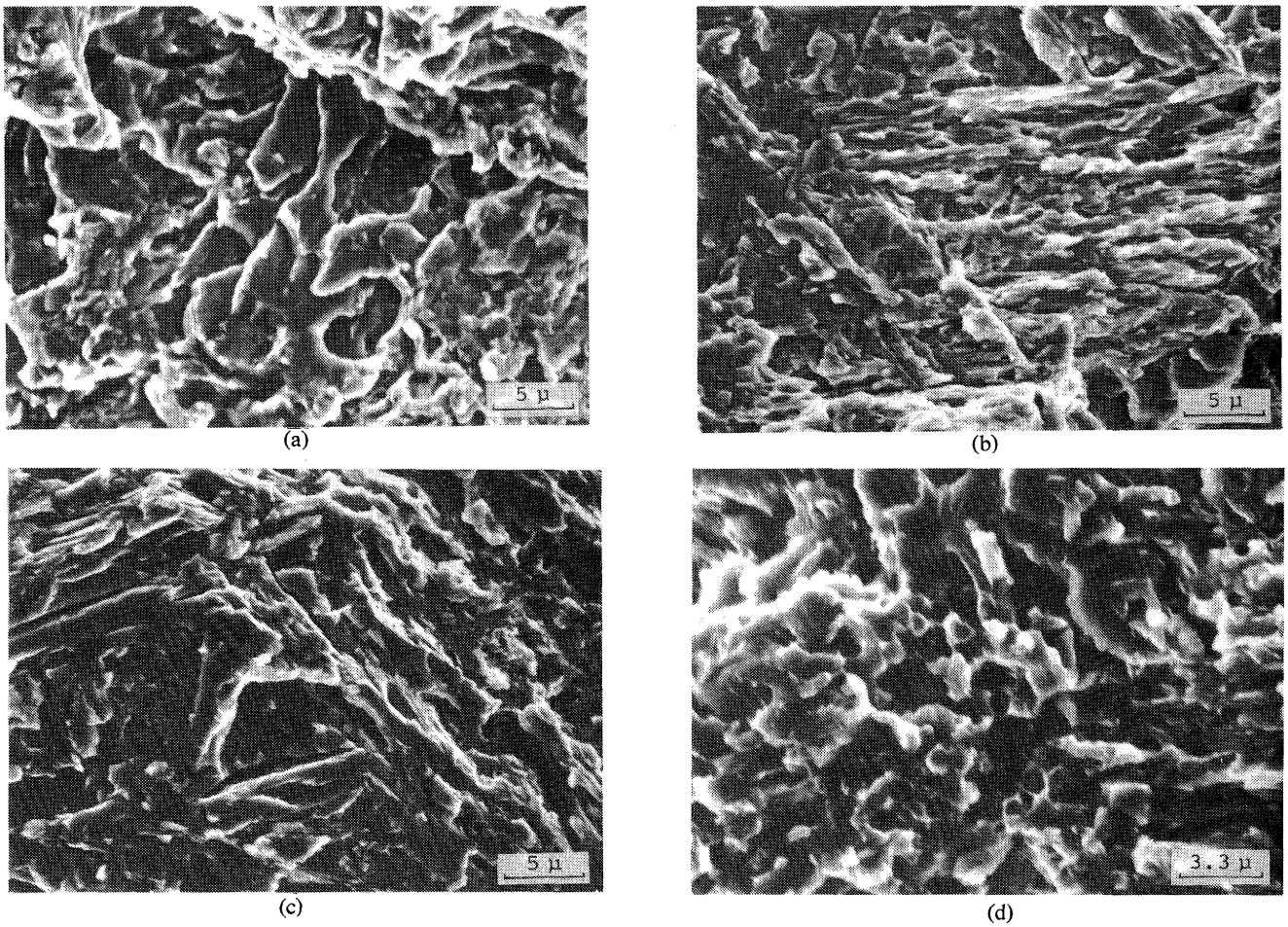

(a) (b) (c) (d)

Fig. 12 Microfractograph of quasi-cleavage region in Group A
(a) S20C, σ=67.3 kg/mm², Tf=27 min, Hd=43.7 ml/100 g
(b) S48C, σ=57.5 kg/mm², Tf=46.8 min, Hd=5.7 ml/100 g
(c) HT80, σ=67.3 kg/mm², Tf=49.1 min, Hd=5.7 ml/100 g
(d) Intermingled fracture of quasi-cleavage and dimple in HT80, σ=77.1 kg/mm², Tf=7.2 min, Hd=16.1 ml/100 g

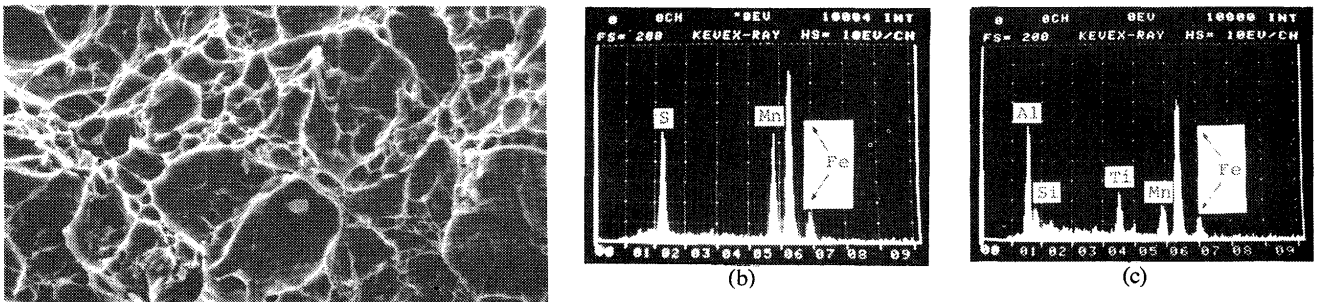

(a) (b) (c)

Fig. 13 Microfractograph of dimple region
(a) An example of dimple fracture in HT80, σ=86.9 kg/mm², Tf=7.2 min, Hd=5.7 ml/100 g
(b) EDX result of inclusion in dimples fractured through heat-affected zone
(c) EDX result of inclusion in dimples fractured through deposited metal

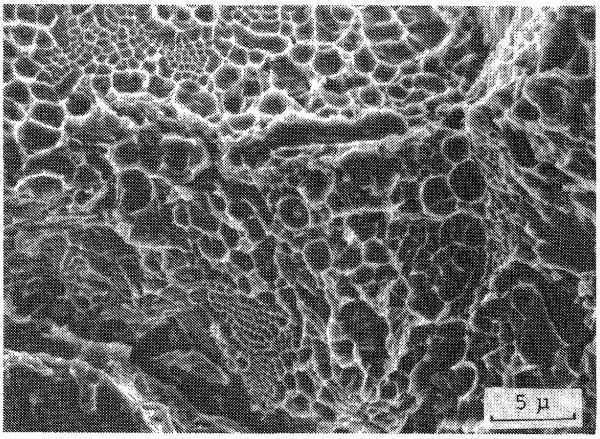

Fig. 14 Example of ductile intergranular fracture within dimple region in S48C, σ=67.3 kg/mm², Tf=1 min, Hd=5.7 ml/100 g

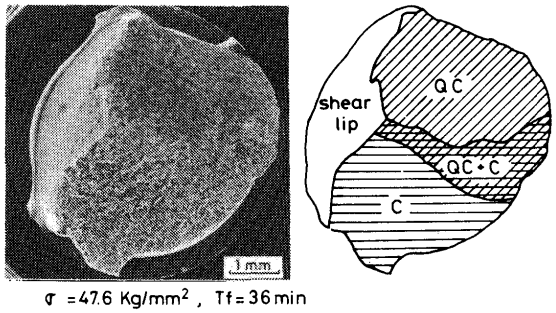

Fig. 15 Typical macrofractograph of S48C, Hd=5.7 ml/100 g

(d) Cleavage Fracture

Cleavage fracture was also observed in the final rapid fracture region of each plain carbon steel, the typical macroscopic feature of which is shown in **Fig. 15.** The microfractograph is shown in **Fig. 16**(a), where river patterns are clearly observed, and thus this fracture is considered to be uneffected by hydrogen. Moreover, it was sometimes observed in each plain carbon steel that the cleavage fracture was partly formed within the quasi-cleavage region as shown in Fig. 16(b). Figure 16(c) shows the direct correspondence between the cleavage fracture part and the microstructure, which reveals that the cleavage fracture was formed at troostite part and that the quasi-cleavage fracture was formed at martensite part. This reason is perhaps that the susceptibility of troostite to hydrogen-induced crack is lower than that of martensite and that the troostite part thus does not crack during propagation of delayed crack and that the part fractures as cleavage type at the final rapid fracture.

Besides, intergranular fracture composed mainly of ductile type and partly of brittle type was sometimes observed in the cleavage region of S48C as seen in

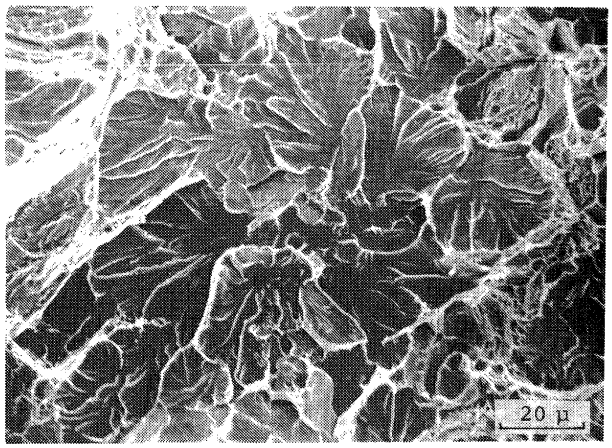

(a)

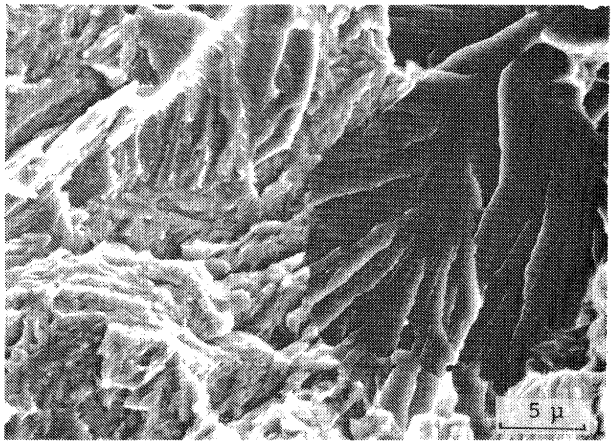

(b)

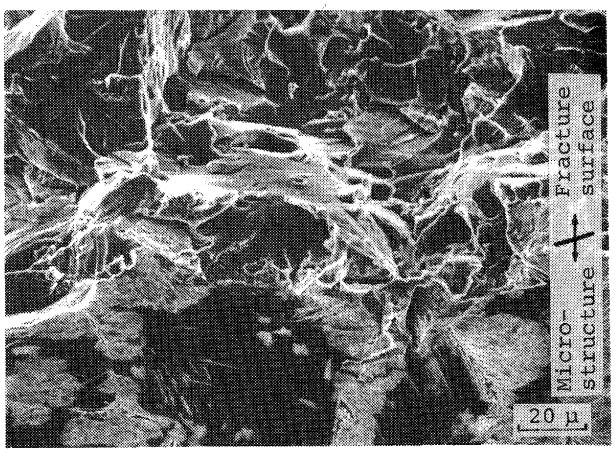

(c)

Fig. 16 Microfractograph of cleavage region in S48C
(a) Typical cleavage fracture, σ=67.3 kg/mm², Tf=1 min, Hd=5.7 ml/100 g
(b) Cleavage fracture within quasi-cleavage region, σ=47.6 kg/mm², Tf=36 min, Hd=5.7 ml/100 g
(c) Direct correspondence between cleavage fracture surface and microstructure, σ=57.5 kg/mm², Tf=46.8 min, Hd=5.7 ml/100 g

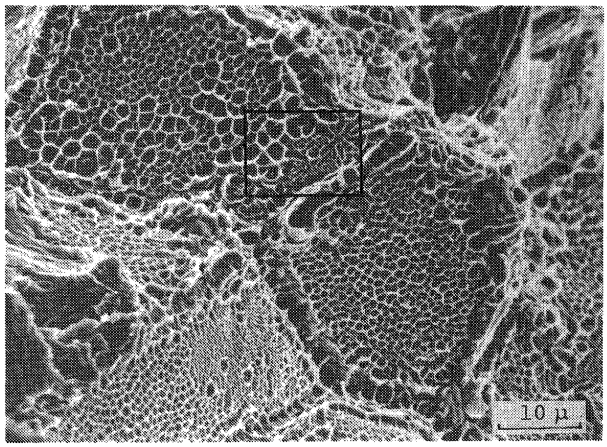

(a)

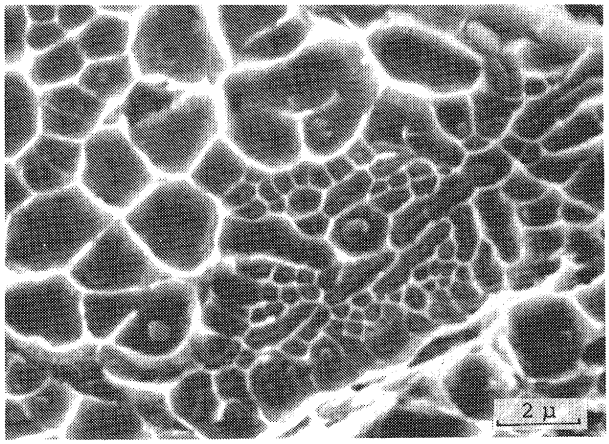

(b)

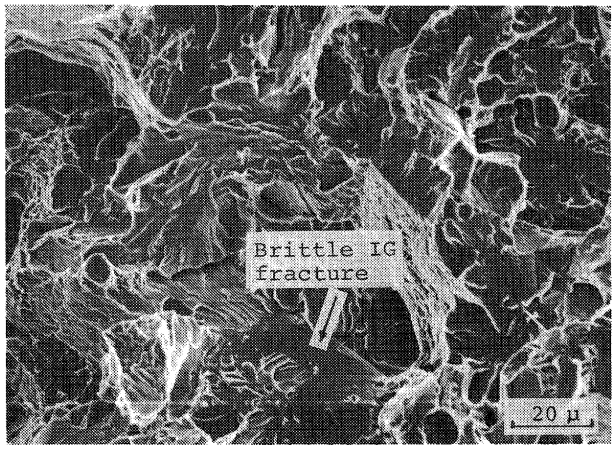

(c)

Fig. 17 Example of intergranular fracture within cleavage region in S48C
- (a) Typical ductile intergranular fracture, σ=67.3 kg/mm², Tf=1 min, Hd=5.7 ml/100 g
- (b) Higher-magnification view of the area of in the rectangle in fractograph (a)
- (c) Brittle intergranular fracture, σ=47.6 kg/mm², Tf=36 min, Hd=5.7 ml/100 g

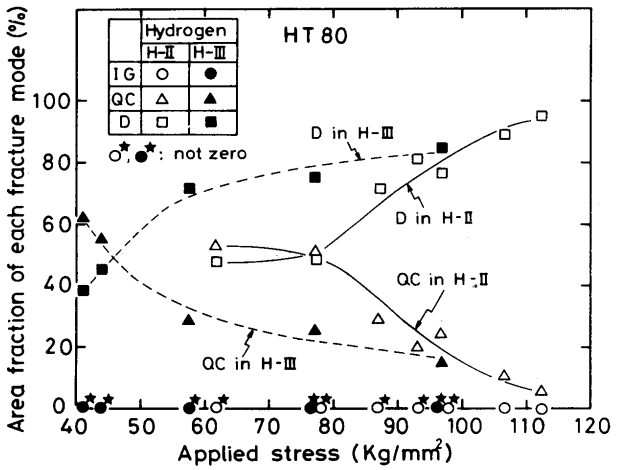

Fig. 18 Area fraction of each fracture region vs. applied stress and diffusible hydrogen content in HT80

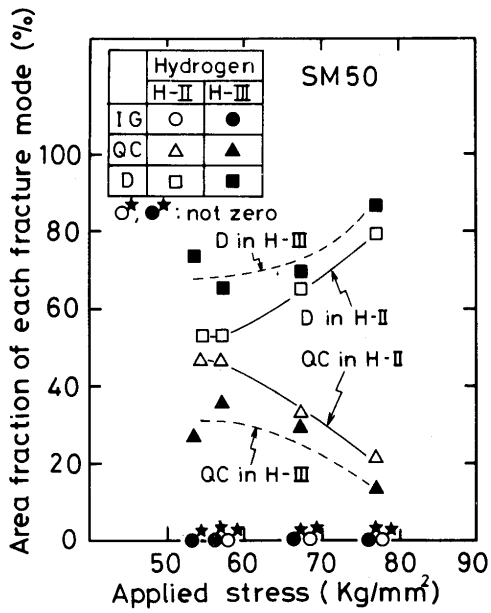

Fig. 19 Area fraction of each fracture region vs. applied stress and diffusible hydrogen content in SM50

Fig. 17. The inclusion in the dimple on the ductile intergranular surface in Fig. 17(b) was MnS type. The reason is considered to be similar to that described in Fig. 14.

There was no cleavage fracture in weldable high strength steels SM50, HT60 and HT80.

(e) Area Fraction of Each Fracture Mode versus Applied Stress and Hydrogen Content

Typical example of dependence of the area fraction of above mentioned fracture surface on applied stress and diffusible hydrogen content is shown in **Fig. 18** in regard to HT80. Figure 18 means that the intergranular fracture is always observed except for two

cases in extremely high applied stress, though the area was very small as seen in Fig. 7 and the dependence on the applied stress and the diffusible hydrogen content was not observed. The area of quasi-cleavage fracture is increased with the decrease in the hydrogen content. The area of dimple fracture has an opposite tendency to the above quasi-cleavage fracture.

The similar tendency is also observed in SM50 as seen in **Fig. 19.** The intergranular fracture as shown in Fig. 10 is always observed, and the dependence of the applied stress and the diffusible hydrogen content is not observed.

The dependences of quasi-cleavage and dimple plus cleavage fractures of S35C, S48C, SM50 and HT80 on the applied stress and on the diffusible hydrogen content were summarized in **Fig. 20.**

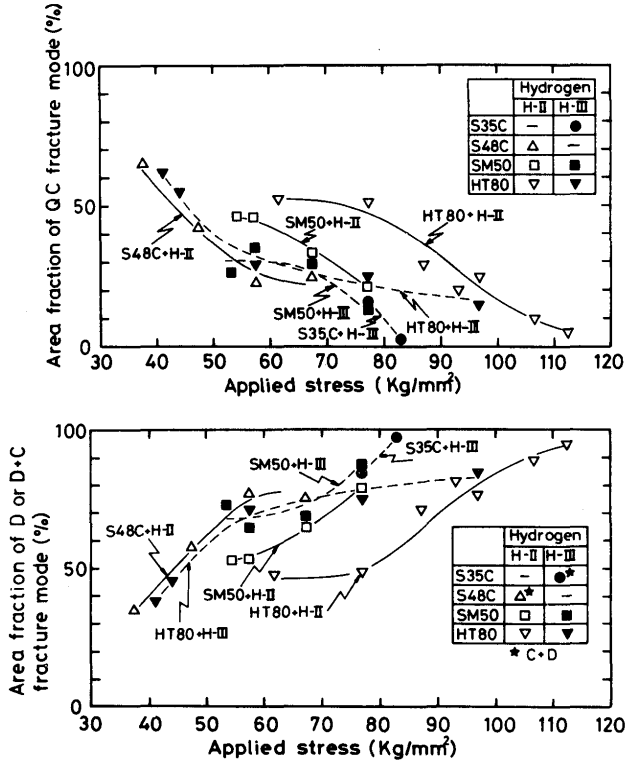

Fig. 20 Area fraction of each fracture region vs. applied stress and diffusible hydrogen content in S35C, S48C, SM50 and HT80

3.3.2 *Fractography of Group B*

Fracture surface of a steel in Group B consisted of three or four modes among intergranular, quasi-cleavage, cleavage and dimple fractures, and the obvious difference with that in Group A is that the intergranular fracture is always contained and occupies a large area on the fracture surface in the higher applied stress.

(a) Intergranular Fracture

Typical examples of the intergranular fracture in

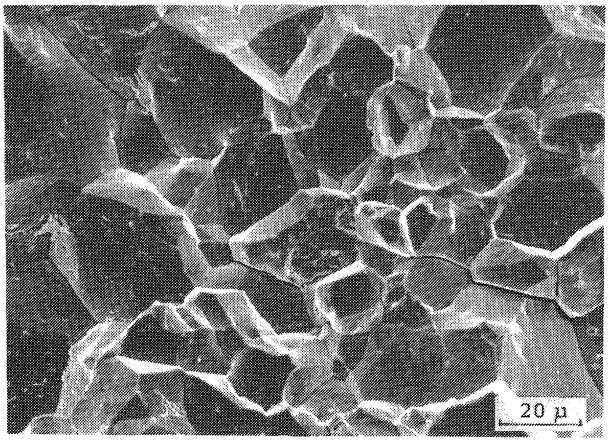

(a)

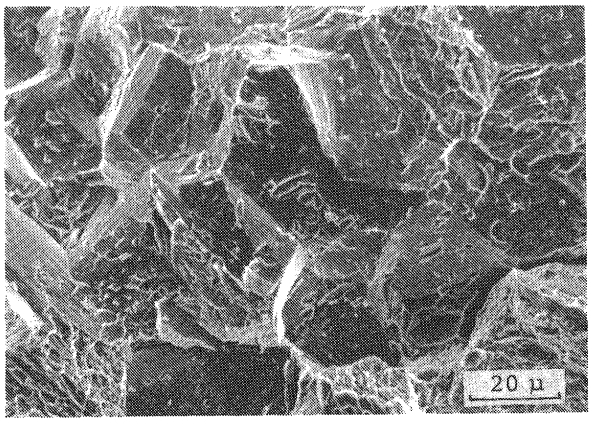

(b)

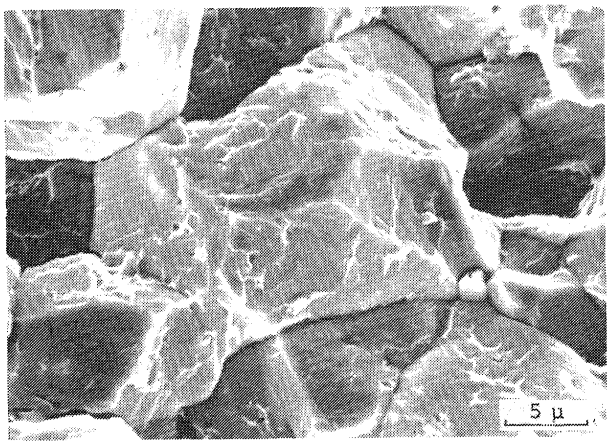

(c)

Fig. 21 Microfractograph of intergranular region of Group B
(a) Smooth grain facets in S50C, σ=47.6 kg/mm², Tf=6 min, Hd=5.7 ml/100 g
(b) Plastic deformation on grain facets in another area of the surface in Fig. 21 (a)
(c) Slightly plastic deformation on grain facets in SNCM8, σ=18.2 kg/mm², Tf=10.8 min, Hd=5.7 ml/100 g

Group B are shown in **Fig. 21,** where very brittle intergranular fracture which has smooth grain facets and secondary cracks along the grain boundaries as

seen in Fig. 21(a) and slightly ductile intergranular fracture which has tear ridges and voids due to plastic deformation as seen in Fig. 21(b) are observed. Macrofractographs in **Fig. 22** show that there is much more intergranular fracture than in Group A and that increase in the applied stress increased the area. This tendency is considered to be contrary to that in a delayed crack. Moreover, the brittle intergranular fracture as seen in Fig. 21(a) is more frequently observed in steels which have very high maximum hardness, especially in SK3 and SUJ2, and in extremely high applied stress. Besides, the brittle intergranular fracture was generally observed at other than neighborhood of the notch.

Furthermore, the very brittle intergranular fracture was hardly observed in SNCM8 and SCM4, and an example in SNCM8 is shown in Fig. 21(c), where slightly plastic deformation on grain facet was observed. Intergranular fracture as seen in Fig. 21(b)

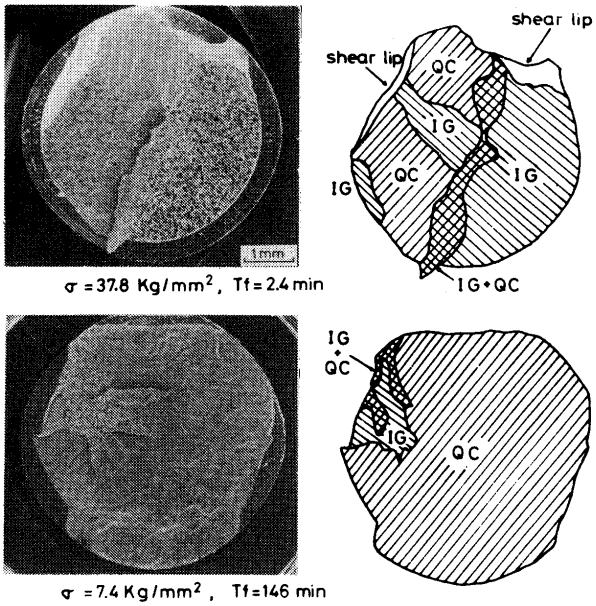

Fig. 22 Variation of macrofractograph of S50C with decreasing applied stress, Hd=5.7 ml/100 g

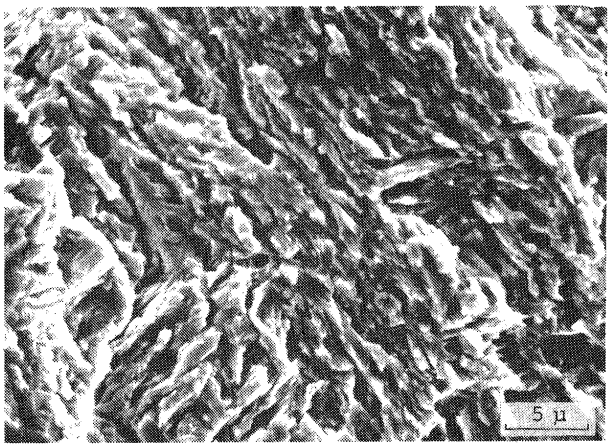

(a)

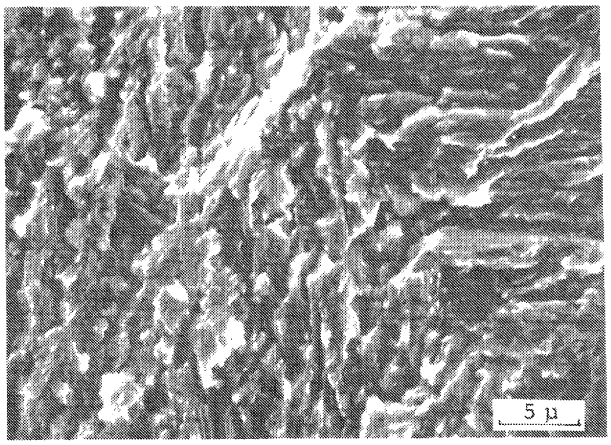

(b)

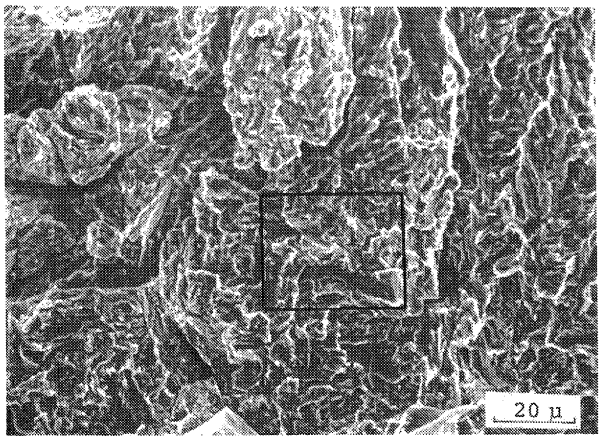

(c)

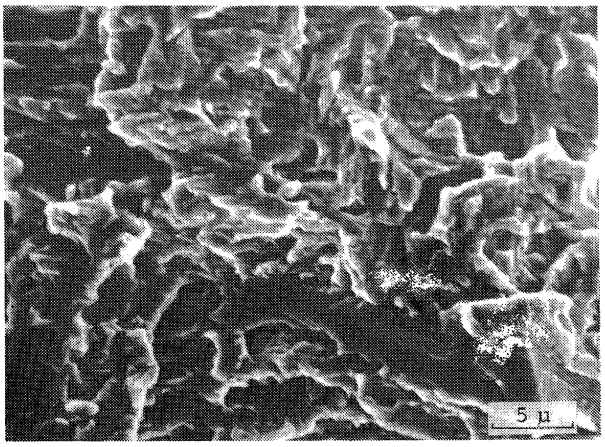

(d)

Fig. 23 Microfractograph of quasi-cleavage region of Group B
(a) S55C, σ=37.8 kg/mm², Tf=1.8 min, Hd=5.7 ml/100 g
(b) SCM4, σ=18.2 kg/mm², Tf=52.8 min, Hd=5.7 ml/100 g
(c) SK3, σ=18.2 kg/mm², Th=79.8 min, Hd=5.7 ml/100 g
(d) Higher-magnification view of the area of in the rectangle in fractograph (c)

was observed near the dimple region in SNCM8 and SCM4.

(b) Quasi-Cleavage Fracture

Typical examples of quasi-cleavage fracture in S55C, SCM4 and SK3 are shown in **Fig. 23**(a), (b) and (c). The quasi-cleavage fracture in S55C and SCM4 are considered to be effected by hydrogen, since tear ridges and secondary cracks are remarkable. The quasi-cleavage fracture in S50C and SNCM8 are also considered to be effected by hydrogen. However, the quasi-cleavage in SK3 and SUJ2 has different features as seen for SK3 in Fig. 23(c) and (d). That is, there are many varieties in size and orientation of each unit facet, and tear ridge and secondary crack are indistinct. Many varieties in size and orientation is considered to be due to the acicular martensite. It is obscure whether the quasi-cleavage of SK3 and SUJ2 is effected by hydrogen or not, since the feature is somewhat similar to that obtained by Charpy impact test as seen in **Fig. 24.** Perhaps the quasi-cleavage fracture is considered to be effected by hydrogen to some extent, considering the delayed crack type curve in Fig. 5.

(c) Cleavage Fracture

Cleavage fracture region was observed in S50C and S55C, an example of which is shown in **Fig. 25.** This is considered to correspond to the final rapid fracture region.

(d) Dimple Fracture

Dimple fracture was sometimes observed in SNCM8 and SCM4. Moreover, mixed feature of dimple and intergranular fracture was sometimes observed in these steels as shown in **Fig. 26.** Inclusion in the dimple is MnS type. There is little dimple fracture in SK3 and SUJ2.

(e) Other Fracture

Hot crack was observed in SK3 together with the intergranular fracture as shown in **Fig. 27.**

(f) Area Fraction of Each Fracture Mode versus Applied Stress

Dependence of above mentioned fracture surface on the applied stress is shown in **Fig. 28.** Increase in applied stress generally increases the area of inter-

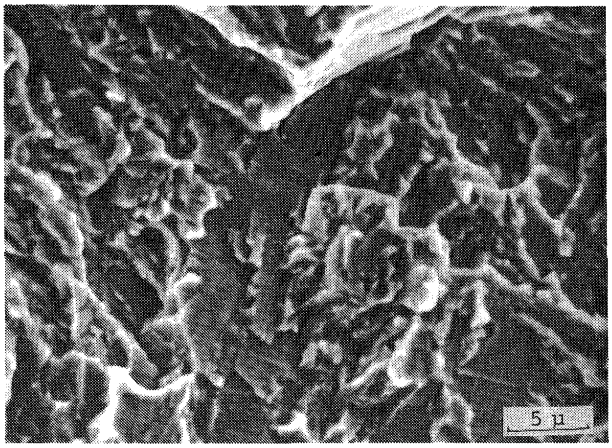

Fig. 24 Quasi-cleavage fracture in a specimen of water-quenched SK3 by a Charpy impact test at room temperature

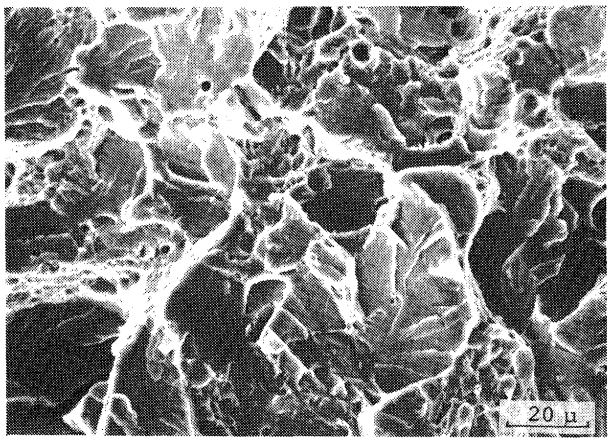

Fig. 25 Microfractograph of cleavage region in S55C, σ=37.8 kg/mm², Tf=1.8 min, Hd=5.7 ml/100 g

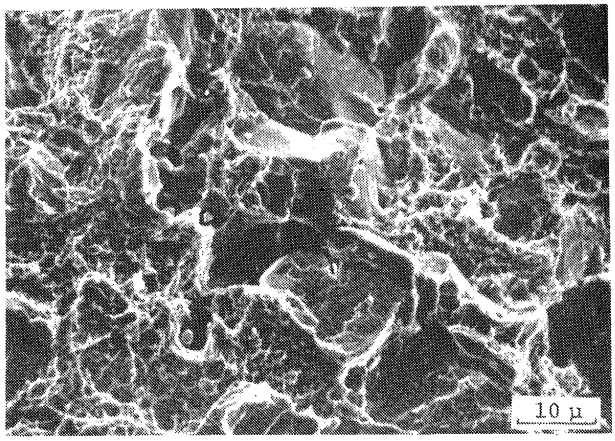

Fig. 26 Intergranular fracture in dimple region in SNCM8, σ=47.6 kg/mm², Tf=0.6 min, Hd=5.7 ml/100 g

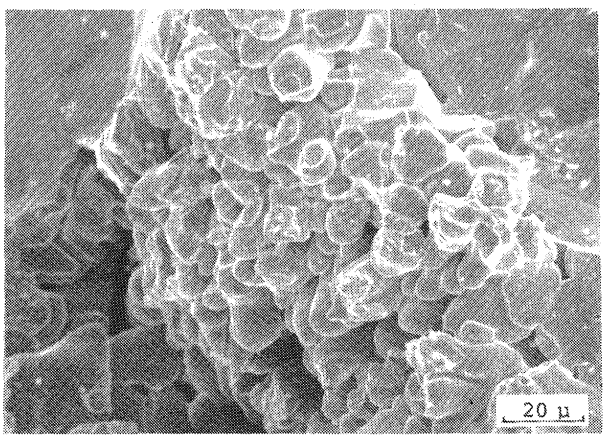

Fig. 27 An example of hot crack in SK3, σ=31.9 kg/mm², Tf=1.1 min, Hd=5.7 ml/100 g

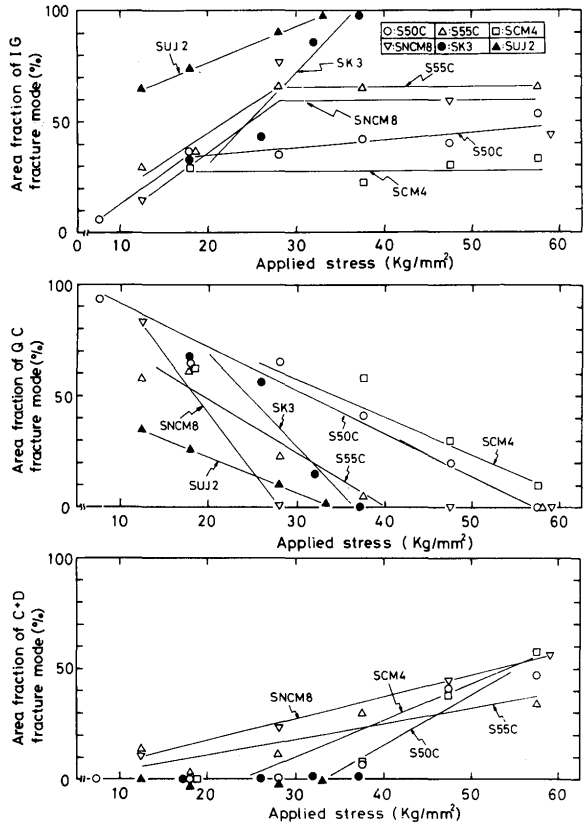

Fig. 28 Relation between applied stress and area fraction of each fracture region in S50C, S55C, SK3, SCM4, SNCM8 and SUJ2

granular fracture as seen in the upper of Fig. 28. This tendency is remarkable in SK3 and SUJ2. Considering this tendency and feature of the intergranular fracture, quenching crack must act on steels in Group B together with hydrogen-induced delayed crack.

Increase in applied stress decreased the area of quasi-cleavage fracture as seen in the middle of Fig. 28, and increases the area of cleavage plus dimple fracture as seen in the lower of Fig. 28 which was considered to be final rapid fracture.

3.4 Synthetic Quenching Crack

Since it is said that quenching crack is generally formed by transformation stress, compulsive fracture by external stress of the specimen during the martensitic transformation is considered to generate the similar fracture surface to that in quenching crack, that is, intergranular fracture of smooth grain facets. Moreover, influence by hydrogen must be negligible by selecting a high cross-head speed.

Then, the compulsive fracture test was intended for S48C, HT60, HT80, S50C, SNCM8, SK3 and SUJ2 by the implant testing apparatus, changing the loading temperature up to 400 °C*. The cross-head speed was about 11 mm/min. As the result, intergranular fracture surface was obtained in each steel in Group B, and was remarkable in higher loading temperature. An example of the fracture is shown in **Fig. 29**(a). On the other hand, intergranular crack was not observed in each steel in Group A except for S48C. Dimple fracture was observed in HT60 and HT80 as seen in Fig. 29(b). Dimple, cleavage and a small amount intergranular fracture were observed in S48C. However, the intergranular fracture was similar to that in Fig. 17(c), and thus is not considered to be due to quenching crack.

This synthetic quenching crack test is considered to be useful for identifying the type of the cold crack of a steel.

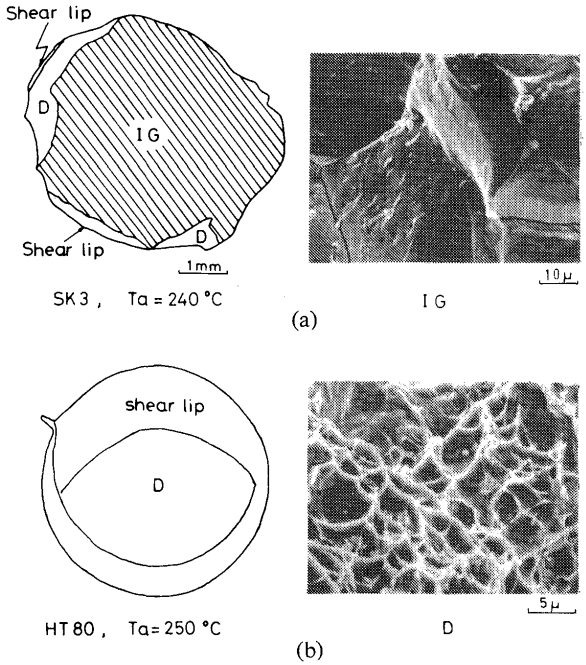

Fig. 29 Examples of fracture surfaces in specimens by Synthetic quenching crack test
(a) Macro-sketch and microfractograph in SK3, loading temperature Ta=240 °C
(b) Macro-sketch and microfractograph in HT80, loading temperature Ta=250 °C

4. Conclusions

Fractographic investigation was made on weld cold crack of various plain carbon steels and low alloy steels, using the implant cracking test and observing a scanning electron microscope. Main conclusions

* Since the cooling rate is considerably high around 400 °C, specimen loaded from 400 °C fractured at about 200 °C.

obtained are as follows:

(1) The fracture mode of hydrogen-induced delayed cracks dominates in plain carbon steels whose carbon content is less than about 0.5% and in weldable high strength steels.

(2) Fracture surface in the conclusion (1) consisted of three or four modes among intergranular, quasi-cleavage, cleavage and dimple fractures. There was no intergranular fracture in plain carbon steels except for in final rapid fracture region, which is considered to be related to the formation of troostite at prior austenitic grain boundaries. The intergranular fracture is always observed in close vicinity to the notch in weldable high strength steel HT80 except for extremely high applied stress, and there is no dependence of the area on the applied stress and the diffusible hydrogen content. Interesting intergranular fracture associated with MnS type inclusion in lamellar segregation was observed in weldable high strength steel SM50. The quasi-cleavage fracture where tear ridges and secondary cracks are formed due to hydrogen is always observed in each steel, and increase in the applied stress and in diffusible hydrogen content decreases the area. Cleavage and dimple fractures are observed in final rapid fracture region.

(3) The fracture mode of quenching crack together with hydrogen-induced delayed crack is obvious in plain carbon steels whose carbon content is more than about 0.50% and medium carbon low alloy steels.

(4) Fracture surface in the conclusion (3) consisted of three or four modes among intergranular, quasi-cleavage, cleavage and dimple fractures, and intergranular fracture was always observed. Increase in the applied stress generally increases the area of intergranular fracture and decreases the area of quasi-cleavage fracture.

(5) It was considered that quenching crack susceptibility can be estimated by compulsive fracture test during martensitic transformation. Observation of the fracture surface by this test revealed the existence of intergranular fracture in steels which belonged to the group in conclusion (3).

References

1) T. Boniszewski, F. Watkinson, R.G. Baker and H.F. Tremlett: "Hydrogen Embrittlement and Heat Affected Zone Cracking in Low-Carbon Alloy Steels with Acicular Microstructure", Brit. Weld. J., Vol. 12 (1965), pp. 14–36.
2) Y. Ito and K. Bessyo: "Cracking Parameter of High Strength Steels Related to Heat Affected Zone Cracking", J. Japan Weld. Soc., Vol. 37, (1968), pp. 983–991, (in Japanese).
3) C.D. Beachem: "A New Model for Hydrogen-Assisted Cracking (Hydrogen Embrittlement)", Met. Trans., Vol. 3 (1972), pp. 437–451.
4) Y. Kikuta, T. Araki and T. Kuroda: "A Study on Mechanism of Hydrogen Embrittlement for Iron and Steel by Means of Electron Fractography", J. Japan Weld. Soc., Vol. 44 (1975), pp. 168–175, (in Japanese).
5) F. Nakasato and F. Terasaki: "Delayed Failure Characteristics of Ultra High Strength Steels", Iron & Steel Inst. Japan, Vol. 61 (1975), pp. 841–855, (in Japanese).
6) T. Kobayashi and I. Aoshima: "Toe and Underbead Cracking in Low-Alloy Steels", Trans. Japan Weld. Soc., Vol. 2 (1971), pp. 70–76.
7) H. Granjion: "The Implant Method for Studying the Weldability of High Strength Steels", Met. Const. & Brit. Weld. J., Vol. 1 (1969), pp. 509–515.
8) J.M. Sawhill, A.M. Dix and W.F. Savage: "Modified Implant Test for Studying Delayed Crack", Weld. J., Vol. 53 (1974), 554s–560s.
9) F. Terasaki and H. Ohtani: "Study of Brittle Fracture Surfaces at Low-Temperature in Relation to Microstructures of Low Carbon Steels", Iron & Steel Inst. Japan, Vol. 58 (1972), pp. 293–305, (in Japanese).
10) A.R. Marder and A.D. Benscoter: "Microcracking in Fe-C acicular Martensite", Trans. ASM, Vol. 61 (1968), pp. 293–298.